Venkatasubramanian, Sathya; Zhang, Chunqing; Laughlin, Leo; Haneda, Katsuyuki; Beach, Mark

Geometry-Based Modeling of Self-Interference Channels for Outdoor Scenarios

Published in:
IEEE Transactions on Antennas and Propagation

DOI:
10.1109/TAP.2019.2896718

Published: 01/05/2019

Document Version
Peer reviewed version

Please cite the original version:
Venkatasubramanian, S., Zhang, C., Laughlin, L., Haneda, K., & Beach, M. (2019). Geometry-Based Modeling of Self-Interference Channels for Outdoor Scenarios. IEEE Transactions on Antennas and Propagation, 67(5), 3297-3307. [8631143]. https://doi.org/10.1109/TAP.2019.2896718

Geometry-based modelling of self-interference channels for outdoor scenarios

Sathya N. Venkatasubramanian, Chunqing Zhang, Leo Laughlin, Katsuyuki Haneda and Mark A. Beach

***Abstract*—In-band full-duplex (IBFD) transmission has the potential to nearly double the throughput by improving the spectral efficiency. The main bottleneck is the self-interference (SI) at the transceiver due its own transmission, which can suppress the desired signal. Compact on-frequency repeaters are suitable candidates for initial implementation of IBFD, where, the design and evaluation of SI cancellation techniques require realistic SI channel models. In this article, we characterise measured MIMO SI channels as a two-dimensional site-specific geometry-based stochastic channel model (GSCM), including smooth walls causing specular reflections, diffuse scatterers along the smooth walls, and mobile scatterers like pedestrians and vehicles. The model provides delay, angular and polarimetric characteristics of the MIMO SI channels, and is validated by comparing the measured and simulated channels in delay, Doppler and spatial domains.**

***Index Terms*—antenna, decoupling, isolation, MIMO, full-duplex.**

I. Introduction

IN-BAND FULL-DUPLEX (IBFD) transceivers [1]–[12], which can simultaneously transmit and receive radio frequency (RF) signals in the same frequency band, have the potential to provide as much as double the capacity compared to traditional half-duplex systems, and reduce latency in wireless networks [6]. Transmitting and receiving on the same time-frequency resource results in strong co-channel *self-interference* (SI), which can be over 100 dB more powerful than the desired receive signal. Time and frequency division duplexing are established methods of *avoiding* co-channel SI, however to achieve IBFD operation, the SI must be mitigated using various techniques to reduce and/or cancel SI at the receiver.

Relays and point-to-point radio links are among the first systems to deploy IBFD technologies [9], [13], [14], with commercial field trials now completed [15] and products implementing IBFD already available [16]. One application for IBFD relays is for outdoor-to-indoor coverage extension, where, for example, in a downlink scenario, a relay is deployed close to a window with receiving antenna(s) decode and/or amplify signals from the base station towards the users inside the building. In this type of system, SI results from direct coupling between the closely spaced transmit (Tx) and receive (Rx) antennas, and from indirect coupling due to multipath propagation between them, i.e., reflections and scattering in the operating environment. Previous results have demonstrated that this multipath propagation can result in significant SI [6], [8].

SI mitigation techniques can, in general, be divided into three categories: SI avoidance over-the-air (OTA) [1], [5], [8], [13], RF SI cancellation [4], [8], [17], and digital baseband SI cancellation [4]. In the OTA SI avoidance, separate antennas are used for Tx and Rx subsystems, thereby providing passive isolation by limiting electromagnetic coupling between the antennas. The effectiveness of the OTA SI avoidance depends on design of the antenna position, pattern, and shielding and/or field absorption techniques [8]. This is then complemented further by RF and digital baseband SI cancellation techniques.

This paper focuses on the OTA isolation, and specifically the measurement and modelling of the SI channel of an IBFD multiple-input-multiple-output (MIMO) relay antenna system. The SI channel includes dynamic multipath coupling due to movement of objects in the physical environment. The RF and baseband SI cancellation techniques need appropriate knowledge of the SI channel, and must thus be both wideband and adaptive over time [11], [18]. The present paper provides understanding of the properties of the SI channel and their models in the time, frequency, polarisation and spatial domains, for the design and evaluation of IBFD relays.

Previous work on SI channel characterisation for an IBFD relay [19] investigated the mean isolation level at 2.6 GHz for indoor deployment, and did not discuss the wideband characteristics of the SI channel. The paper [20] reports indoor wideband SI channels between 2.45 to 2.75 GHz based on measurements, but still lacks the spatial and Doppler characteristics. This paper extends the work [20], with the following three-fold major advances.

1) Performing additional measurements to cover various deployment scenarios of IBFD relays,
2) Characterising the SI channels in terms of delay, Doppler, spatial and polarisation domains in addition

Manuscript received XXX....

Sathya N. Venkatasubramanian and Katsuyuki Haneda are with the Department of Electronics and nanoengineering, Aalto University, School of Electrical Engineering, Espoo, Finland

Chunqing Zhang, Leo Laughlin, and Mark A. Beach are with the Department of Electrical and Electronic Engineering, University of Bristol, Bristol, United Kingdom.

The research work leading to these results was funded by the Academy of Finland, under the project "In-band Full-Duplex MIMO Transmission: A Breakthrough to High-Speed Low-Latency Mobile Networks", the Finnish Funding Agency for Technology and Innovation, Tekes, under the project "Full-Duplex Cognitive Radio: Technology and Application to Cognitive M2M Communications", the Aalto ELEC doctoral school, Finland, the UK Engineering and Physical Sciences Research Council, under the project "Scalable Full-Duplex Dense Networks (SENSE)", and the University of Bristol, UK.

Color versions of one or more of the figures in this paper are available online at http://ieeexplore.ieee.org.

Digital Object Identifier:

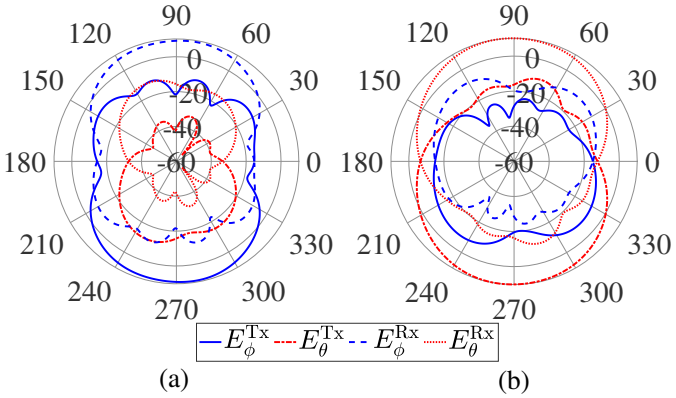

Fig. 1. Simulated radiation patterns of a single Tx-Rx antenna pair in the azimuth plane for (a) horizontally polarised antennas, and (b) vertical polarised antennas.

to the already-reported wideband characteristics; and finally,

3) Establishing a site-specific geometry-based stochastic channel model (GSCM) in a similar spirit as [21], [22], as a versatile tool to reproduce the SI channel over spatial, temporal, delay and polarisation domains jointly.

The remainder of this paper is organised as follows. Section II describes the measurement setup, modes and scenario. Section III describes the measured SI channel characteristics, which is then modelled as a site-specific GSCM as described in Section IV. Section V describes the channel model validation and Section VI concludes the paper.

II. SI Channel Measurements

A. Antenna Array

For the wideband and time-varying MIMO SI channel measurements, a compact relay antenna system consisting of back-to-back patch antennas was chosen. It has dimensions of $180 \times 150 \times 57\text{mm}^3$ as previously reported in [20]. The relay comprises two ground planes spaced 47 mm apart using nylon screws, with two dual-polarised patch antennas on either side facing opposite directions, corresponding to four feeds on each side. We assume that the four feed ports on one side serve for Tx, and another four on the other side for Rx. In total, we have $4 \times 4 = 16$ coupling channels between the Tx and Rx feeds. Of these, eight are between Tx and Rx antenna feeds with the same polarisation, and the other eight are between antenna feeds with orthogonal polarisations.

The individual antenna feeds have input matching better than -6 dB over around 300 MHz bandwidth across 2.6 GHz. The mutual coupling between the antenna feeds in the anechoic chamber, which refers to the direct coupling in the SI channel, varies between -40 to -80 dB for different antenna combinations. Fig. 1 shows the simulated azimuth radiation patterns of the horizontally (H) and vertically (V) polarised Tx and Rx antennas. The antennas have a main lobe gain of 9.3 dBi in the respective broadside directions. Due to the back-to-back structure of the relay, their broadside points in opposite directions.

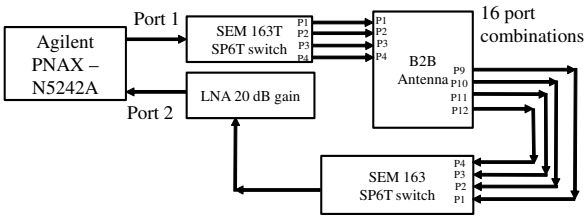

Fig. 2. Schematic of the SI measurement setup with the 4×4 MIMO back-to-back (B2B) antenna connected to the VNA using SP6T switches.

B. SI Channel Measurements

The dynamic wideband MIMO SI channel measurements were performed using an Agilent PNAX-N5242 Vector Network Analyzer (VNA). The VNA performs continuous-wave measurements of channels between 2.45 and 2.75 GHz with 0.5 MHz spacing. The measurement setup is described in Fig. 2. Port 1 of the VNA was used as a transmitting port and connected to antenna feeds 1-4 through a SP6T switch (Narda SEM163T). The two unused ports of the RF switch were terminated by 50 Ω loads. Feeds 9-12 were connected to another SP6T switch (Narda SEM163) in a similar configuration, and was then connected to a low noise amplifier (LNA) with 20 dB gain before it is fed to Port 2 of the VNA. The scattering parameters, S_{21} of the SI channel were measured for different antenna combinations over time. The switches were mounted at the base of the antenna tripod, and were controlled using a custom microcontroller and logic circuit with a serial RS-232 interface. The switches and VNA were interfaced using MATLAB codes. The effect of the internal circuits of the VNA, cables, and switches were removed in the data post-processing using back-to-back calibration.

C. Measurement Modes

In this section, we describe the different modes of the measurement setup to model the delay and Doppler characteristics.

1) Static mode: The multipath SI channel measurements were performed at multiple positions, i.e., different antenna locations and heights. The S_{21} was measured sequentially for different feed combinations using the RF switches to obtain the 4×4 MIMO SI channels. A complete measurement of a MIMO channel takes 640 ms including the switching delay. At each antenna position, the MIMO channel was measured 10 times.

2) Doppler mode: In order to characterise the temporal fading characteristics of the SI channel, the S_{21} is repeatedly measured at higher temporal sampling rates than the static mode. Because of the relatively slow RF mechanical switches, these measurements were conducted only for one antenna feed combination at a time. Moreover, due to the limited memory available on board the VNA, there is a trade-off between the temporal sampling rate and the duration of the measurement. The VNA was configured to use a *segmented sweep* mode, in which multiple sweeps are stored into the same trace buffer, avoiding accessing the memory during the sweeps. In this mode the sampling rate is limited only by the sweep time

and the local oscillator fly-back time. For the 300 MHz bandwidth and 0.5 MHz frequency resolution, this configuration allows us to measure channels every 7 ms. This leads to a Doppler bandwidth of 142 Hz, which corresponds to 71 Hz maximum Doppler shift. However, due to the limited trace buffer size, the number of sweeps was also limited to 20 per measurement, with each sweep repeatedly sampling across the entire bandwidth 50 times, resulting in a sampling duration of $7\text{ms} \times 50 = 350$ ms. This corresponds to 2.86 Hz resolution of the Doppler spectra. Due to the large measurement time taken for the Doppler characterisation, only two feed combinations, one *co-* polarised and one *cross-* polarised were measured.

D. Measurement Scenario

The SI channels were measured outside a building window at the street level. The measurement sites were on Park Row, Bristol, adjacent to the Merchant Venturers Building at the University of Bristol. This street has three story buildings on both sides of the road, forming a street canyon. Measurements were taken at three locations adjacent to the window, repeated at 11 antenna heights between 170 cm and 190 cm with 2 cm increment, resulting in 33 measurement positions in this measurement scenario. The antenna was oriented with the main beams facing out of the window/into the room. The antenna was located 30 cm in front of the windows.

III. SI Channel Characteristics

In this section, the delay, temporal and spatial domain characteristics of the measured SI channels are discussed by means of the power delay profile (PDP), power Doppler spectra (PDS) and antenna correlation.

A. Delay Domain Characteristics

1) Derivation of PDPs: The static mode measurements described in Section II-C are used for deriving the PDP. The wideband time-varying MIMO SI channels are described by transfer function $H_{ij}(f,t,p)$, where i and j are the Rx and Tx antenna indices, respectively, f denotes the measurement radio frequency index, t refers to the measurement time index at the antenna position, $1 \leq t \leq 10$, corresponding to 10 realizations of $\boldsymbol{H}(f,t,p)$ obtained over time as described in Section II-C; p refers to the antenna position index, $1 \leq p \leq 33$ as described in Section II-D.

The channel impulse response (CIR) of each antenna combination $h_{ij}(m,t,p)$ is obtained by the Inverse Fast Fourier transform (IFFT) of $H_{ij}(f,t,p)$ with the Hann window; m refers to the delay bin index defined at every 3.33 ns corresponding to 300 MHz measurement bandwidth. The Hann window was chosen as it has low levels of signal leakage in the delay domain, allowing weaker parts of the SI channel to be detected properly. The amplitude of each impulse response is then scaled with a factor of 0.5 to account for the reduction of the main-lobe power due to the Hann window.

The PDP for each feed combination is obtained from the CIRs as

$$PDP_{ij}(m) = E_{t,p}\{|h_{ij}(m,t,p)|^2\}, \quad (1)$$

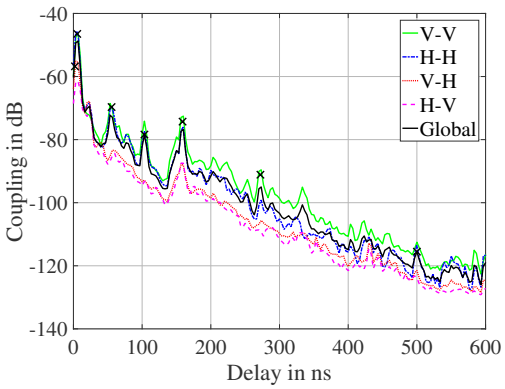

Fig. 3. Measured PDPs indicating *polarisation-specific* PDPs obtained from the ensemble average of the PDPs with the corresponding antenna polarisations and the *global* PDP with specular peaks.

thereby removing the effect of small scale fading; $E_{t,p}\{\cdot\}$ refers to the ensemble average with respect to realizations over time t and position p. A single PDP for each antenna combination is therefore defined for the measurement *scenario*.

The *polarisation-specific* PDPs i.e., for *co-* polarised feed combinations, V-V, H-H, and *cross-* polarised feed combinations, V-H and H-V, are calculated as the ensemble average of the PDPs between the respective feed combinations. The *global* PDP is derived as the ensemble average of the PDPs over all the feed combinations.

A peak in the PDP is identified at a particular delay bin if the power in the delay bin is 3 dB larger than the 7-bin moving average of the PDP, centered at the delay bin. In addition, the first three delay bins, i.e., 0 ns, 3.33 ns and 6.67 ns are identified as peaks. When the peak delay bins are detected, accurate peak delays and powers are determined by fitting the local PDP shape around the peak delay bin with a Sinc function for interpolation. The Sinc function in the delay domain corresponds to a rectangular frequency window of the transfer function. For the interpolation, the PDP is calculated from the CIRs that are obtained from the transfer function using a rectangular window instead of the Hann window.

2) Scatterer identification: Fig. 3 shows the measured *global* and *polarisation-specific* PDPs. The objects causing the specular peaks are identified based on the geometry of the measured scenario and matching them to the corresponding delays of the peaks. The main objects causing the specular reflections are indicated in Fig. 4, which includes the room walls indoors next to the antenna as well as the buildings/objects on the other side of the road. The measured polarisation specific PDPs shown in Fig. 3 indicates that the power for the H-H polarisation is smaller than the V-V polarisation, which can be attributed to the radiation pattern of the antennas as shown in Fig. 1.

3) Delay dispersion: The delay dispersion of the SI channel, represented by the mean delay, τ_{m} and the RMS delay spread, τ_{rms} are calculated from the *global* and *polarisation-specific* PDPs in the manner defined in [23]. Since the SI cancellation aims to suppress the SI to the noise floor, all delay bins with power above the noise floors are used in their

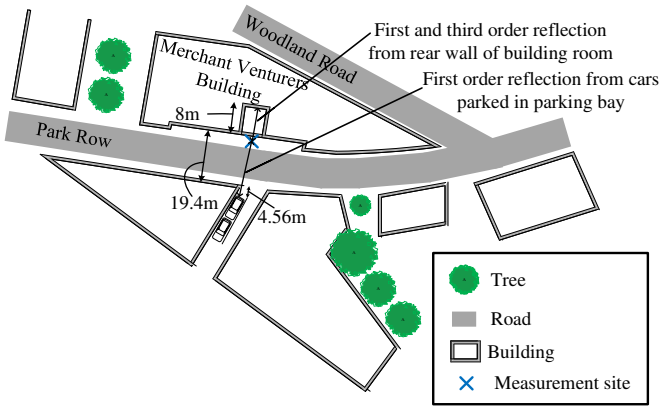

Fig. 4. Schematic of measurement site with antenna deployed outside building window. The specular paths are reflected from the rear wall of the room inside the building, and vehicles parked facing the antenna on the opposite side of the road. In addition, the glass window near the antenna location causes specular reflection arriving in the initial delay bins.

calculation. The noise threshold is given by $P_{\text{th}} = P_{\text{n}} + 6$ dB where P_{th} and P_{n} are noise threshold and estimated noise from the PDPs, respectively. The *global* RMS delay spread is 10.7 ns with mean delay of 6.5 ns indicating that most of the SI power arrives within the first four delay bins.

4) Wideband fading characteristics: The wideband fading characteristics of the SI channel is modelled by estimating the Ricean K-factor of each delay bin through the moment-based method [24]. The fading realizations come from the CIRs of the MIMO channel at different antenna positions. The magnitudes of the CIRs are normalized to that of the PDP of the corresponding antenna combination as

$$a_{ij}(m,t,p) = |h_{ij}(m,t,p)|^2 / PDP_{ij}(m). \tag{2}$$

The Ricean K-factor for the first two delay bins at 0 ns and 3.33 ns is 5.1 dB and 0.3 dB respectively, due to the direct component. The remaining delay bins exhibit Rayleigh fading, i.e., $K \leq 0$ dB due to several multipaths arriving at the same delay bin.

B. Doppler characteristics

Moving objects such as pedestrians and cars in the surrounding environment of the IBFD relay device causes Doppler effects to the SI channel, resulting in its time-variation. The Doppler measurement mode described in Section II-C was therefore our main interest in this subsection. The transfer functions for the measured *co-* and *cross-* polarised feed combinations, $H_{\text{co}}(f,t,p,n)$ and $H_{\text{cross}}(f,t,p,n)$ respectively, are defined in the same manner as Section III-A, except for $n = 1, 2, ..., 20$ referring to the measurement sweep index at the same antenna position as described in Section II-C.

Having obtained the corresponding CIRs, $h_{\text{co}}(m,t,p,n)$ and $h_{\text{cross}}(m,t,p,n)$ using the IFFT similarly to Section III-A, the spreading functions [23], $S_{\text{co}}(m,\nu,p,n)$ and $S_{\text{cross}}(m,\nu,p,n)$ are derived by applying the FFT to the series of CIRs over time, $1 \leq t \leq 50$, sampled every 7 ms at each position, leading to the delay-Doppler representation of the channel with Doppler frequency ν. The PDS for the *co-* and *cross-* polarised channels is obtained by incoherently averaging the spreading functions as

$$\begin{aligned} PDS_{\text{co}}(m,\nu,p) &= E_n\{|S_{\text{co}}(m,\nu,p,n)|^2\}, \\ PDS_{\text{cross}}(m,\nu,p) &= E_n\{|S_{\text{cross}}(m,\nu,p,n)|^2\}, \end{aligned} \tag{3}$$

where $E_n\{\cdot\}$ denotes the ensemble average over the measurement sweeps at the same antenna position. The mean Doppler shift, ν_{m} and the RMS Doppler spread, ν_{rms} are calculated at each delay bin and antenna position as defined in [23], considering Doppler bins with power greater than the noise floor of the measurements. The mean of ν_{m} and ν_{rms} across antenna positions, $\overline{\nu_{\text{m}}}(m)$ and $\overline{\nu_{\text{rms}}}(m)$ respectively, is then calculated at each delay bin for the *co-* and *cross-* polarisations. The *global* mean Doppler shift and RMS Doppler spread are finally given by the mean of $\overline{\nu_{\text{m}}}(m)$ and $\overline{\nu_{\text{rms}}}(m)$ over the *co-* and *cross-* polarised feed combinations. Fig. 5 shows the *global* mean Doppler shift and RMS Doppler spread as well as the *co-* and *cross-* polarised RMS Doppler spreads. The Doppler spreads upto 40 ns delay is primarily due to pedestrian movement, while beyond 40 ns delay, the Doppler spread is attributed to both pedestrian and vehicular movement. The RMS Doppler spreads for the *co-* and *cross-* polarisations follow a similar pattern. Also, a wooden door was ~ 2 m away from the antenna site, which was opened and closed frequently, with people walking towards and away from the antenna. This can cause additional Doppler spread in the initial delay bins.

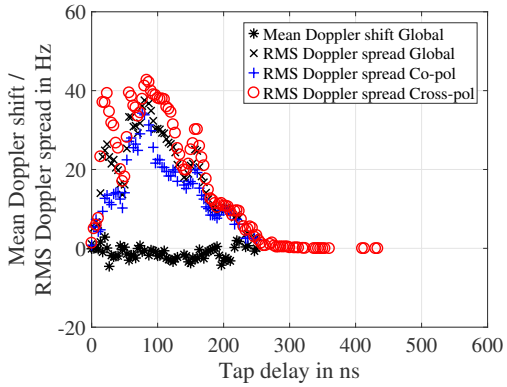

Fig. 5. Measured mean Doppler shift and RMS Doppler spreads.

C. Spatial characteristics

We finally derive the narrowband antenna correlation of the SI MIMO channel as a measure of spatial and polarimetric characteristics. The static mode measurements are used for the analysis.

The narrowband antenna correlation between the j-th and k-th Tx antenna ρ_{jk}^{Tx} is defined as

$$\rho_{jk}^{\text{Tx}}(t,p) = \frac{\sum_{i=1}^{4} (|H_{ij}| - \overline{|H_j|})(|H_{ik}| - \overline{|H_k|})}{\sqrt{\sum_{i=1}^{4} (|H_{ij}| - \overline{|H_j|})^2} \cdot \sqrt{\sum_{i=1}^{4} (|H_{ik}| - \overline{|H_k|})^2}}, \tag{4}$$

where i refers to the Rx antenna index, $\overline{|H_j|} = E_{f,i}\{|H_{ij}|\}$. For convenience, the time, t, frequency, f, and position index, p, dependence is suppressed in the right hand side of (4). We then calculated the mean antenna correlation over time and position as

$$\overline{\rho}_{jk}^{\mathrm{Tx}} = E_{t,p}\{\rho_{jk}^{\mathrm{Tx}}(t,p)\}. \tag{5}$$

The narrowband correlation between the Rx antenna elements is calculated in a similar manner. The antenna correlation is found less than 0.6, indicating large angular dispersiveness of the channel, hence possibly leading to limited performance of eigenmode-based SI mitigation techniques [25].

IV. SI Channel model

A site-specific GSCM is developed based on the SI channel characteristics described in Section III for the outdoor deployment of IBFD relays. First, the site-specific geometry is defined, and then a method to reproduce the SI channel as a sum of propagation paths is given. Finally, the implementation recipe is enumerated to generate dynamic wideband MIMO SI channel.

A. Geometry description

The schematic of the proposed two-dimensional geometry is illustrated in Fig. 6. It comprises of smooth building walls on both sides of the road, as well as the smooth walls of the room inside the building next to the antenna deployment location. In addition, we model diffuse scatterers placed adjacent to the smooth walls, and mobile scatterers, i.e., pedestrians and vehicles on the road.

The length and width of the road is defined along the x- and y-axes, respectively. The coordinate limits of the geometry along the y dimension is determined by the road width W_{road} and the room depth D_{room} next to the antenna, as shown in Fig. 6. The origin is located at the centre of the road. The coordinate limits along the x dimension is determined by the maximum delay $\tau_{\max}$ due to first order diffuse scattering from objects on both sides of the antenna, along the x axis. Since the Tx and Rx are co-located, $x_{\min} = x_{\mathrm{Tx}} - \tau_{\max} c/2$ and $x_{\max} = x_{\mathrm{Tx}} + \tau_{\max} c/2$ where x_{Tx} corresponds to the x-coordinate of the Tx and c is the velocity of light. The following defines characteristics of paths due to different walls and scatterers.

1) Smooth walls: The building walls on both sides of the road are at $y = \pm W_{\mathrm{road}}/2$ and extend upto $x_{\min}$ and $x_{\max}$. The walls of the room behind the antenna are also defined as smooth walls with dimensions $W_{\mathrm{room}} \times D_{\mathrm{room}}$. Each wall is assigned corresponding permittivities and normal vectors. Up to N_{w}-th order reflections from the walls are considered. The complex signal amplitude of the l-th reflected path $\boldsymbol{\alpha}_{\mathrm{wall}}^{l}$ is

$$\boldsymbol{\alpha}_{\mathrm{wall}}^{l} = \left(\frac{\lambda}{4\pi d_l}\right)^{n_{\mathrm{l}}/2} e^{j\xi_l} \prod_{n_{\mathrm{w}}=1}^{N_{\mathrm{w}}} \begin{bmatrix} \Gamma_{\mathrm{VV}}^{(n_{\mathrm{w}})} & 0 \\ 0 & \Gamma_{\mathrm{HH}}^{(n_{\mathrm{w}})} \end{bmatrix}, \tag{6}$$

where λ is the free space wavelength and d_l is the propagation path length; $\Gamma_{\mathrm{VV}}^{(n_{\mathrm{w}})}$ and $\Gamma_{\mathrm{HH}}^{(n_{\mathrm{w}})}$ are the Fresnel reflection coefficients at the n_{w}-th interaction of the path with the smooth wall for the respective polarisations. A random phase $\xi_l \sim U[0, 2\pi]$ is added to each path to account for the phase change due to ground reflections of the corresponding paths. The path loss exponent, n_{l} is defined as

$$n_{\mathrm{l}} = \begin{cases} 2.2 & \text{if } d_l \le d_{\mathrm{break}} \\ 3.3 & \text{if } d_l > d_{\mathrm{break}} \end{cases}, \tag{7}$$

where $d_{\mathrm{break}} = 4{h_{\mathrm{ant}}}^2/\lambda$ is the breakpoint distance where the ground begins obstructing the first Fresnel zone; h_{ant} refers to the Tx/Rx antenna height. The higher path loss exponent $n_{\mathrm{l}} > 2$ is a reasonable estimate considering the low antenna height, obstruction of paths' first Fresnel zone due to the ground as well as reflections from the ground [26].

In addition, if the signal penetrates through the glass windows near the antenna, which produces reflected paths from the deeper wall in the room as observed in the measurements, the corresponding path undergoes additional penetration loss, determined by the polarimetric transmission coefficients. In addition, 10 dB losses are added to paths if they are shadowed by the relay antenna itself; such paths occur when thinking of twice-reflection on both sides of the walls for example. The 10 dB additional loss is a reasonable estimate when considering the shadowed Fresnel zone size at 2.6 GHz. The angle-of-arrival (AoA) ϕ_{AoA}^{l}, and angle-of-departure (AoD) ϕ_{AoD}^{l} of the l-th reflected path is calculated at the co-located Tx/Rx location.

2) Diffuse scatterers adjacent to smooth walls: Next, we consider diffuse scatterers located on, and next to smooth walls, which correspond to objects such as sign boards and rough brick walls. These diffuse scatterers are located at a small distance, i.e. 5 cm in front of the smooth walls and are uniformly spaced along them with density $\lambda_{\mathrm{diffuse}}$. Each diffuse scatterer is assigned a Radar Cross Section (RCS) with isotropic scattering. Due to the cluttered street canyon environment as well as the operating radio frequency of 2.6 GHz, both first order and second order diffuse scattering is considered. The polarimetric complex amplitude of a path arising from the s-th diffuse scatterer is given by

$$\boldsymbol{\alpha}_{\mathrm{diffuse}}^{s} = \frac{\lambda}{4\pi {d_s}^2}\sqrt{\frac{\sigma_s}{4\pi}} \cdot \boldsymbol{\gamma}_s, \tag{8}$$

where d_s corresponds to the distance of the scatterer from the co-located Tx/Rx location and σ_s is the RCS of the corresponding scatterer. The distance term is squared indicating equal path length from the Tx to the scatterer and from the scatterer back to the Rx; $\boldsymbol{\gamma}_s$ denotes the polarisation matrix, defined as

$$\boldsymbol{\gamma}_s = \begin{bmatrix} e^{j\xi_{11}^{s}} & \frac{e^{j\xi_{12}^{s}}}{\sqrt{CPR \cdot XPD_{\mathrm{H}}}} \\ \frac{e^{j\xi_{21}^{s}}}{\sqrt{XPD_{\mathrm{V}}}} & \frac{e^{j\xi_{22}^{s}}}{\sqrt{CPR}} \end{bmatrix}, \tag{9}$$

where CPR, XPD_{V} and XPD_{H} refer to the *co-* and *cross-*polar power ratios between the vertical and horizontal polarizations as given by

$$CPR = \frac{P_{\mathrm{VV}}}{P_{\mathrm{HH}}}, \quad XPD_{\mathrm{V}} = \frac{P_{\mathrm{VV}}}{P_{\mathrm{HV}}}, \quad XPD_{\mathrm{H}} = \frac{P_{\mathrm{HH}}}{P_{\mathrm{VH}}}. \tag{10}$$

The phase of each element of the polarization matrix is assigned randomly for each of the scattered paths, $\xi_{ij}^{s} \sim U[0, 2\pi]$.

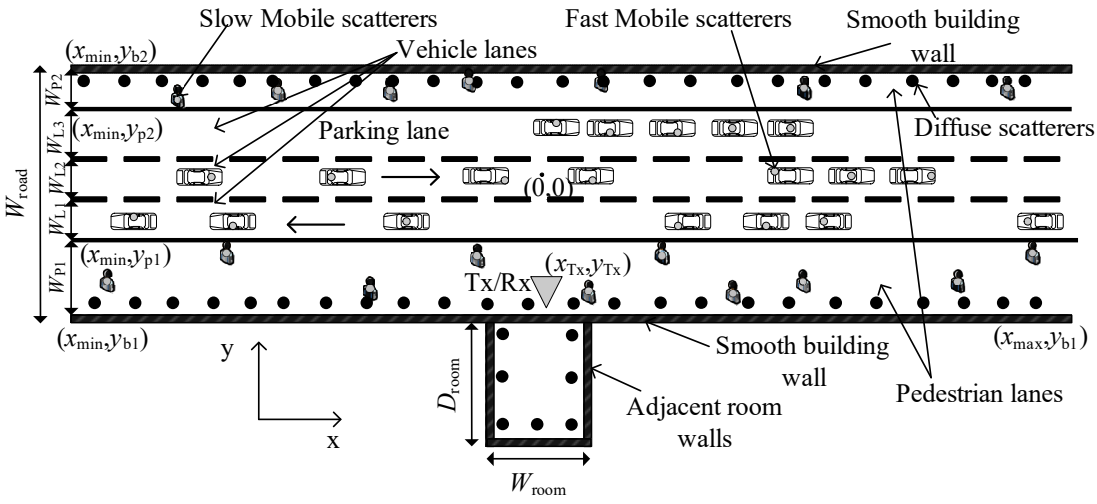

Fig. 6. Schematic of the proposed site-specific geometry for the dynamic wideband MIMO SI channel model. It comprises smooth walls, diffuse and mobile scatterers. The x- and y-coordinates and the scatterer density are representative and not to scale; $W_{\mathrm{P}i}$ and $W_{\mathrm{L}i}$ denotes width of the i-th pedestrian and vehicle lanes including parking lanes respectively. Each mobile and diffuse scatterer is associated with a corresponding RCS.

The complex polarimetric amplitude of the second order scattered paths from the diffuse scatterers s_1 and s_2 is given by

$$\boldsymbol{\alpha}_{\mathrm{diffuse}}^{s_1 s_2} = \frac{\lambda}{4\pi d_{s_1} d_{s_2} d_{s_{12}}} \frac{\sqrt{\sigma_{s_1}\sigma_{s_2}}}{4\pi} \cdot \boldsymbol{\gamma}_{s_1 s_2}, \tag{11}$$

where d_{s_1} and d_{s_2} correspond to the distance between the co-located Tx/Rx antennas and the scatterers s_1 and s_2 respectively, and $d_{s_1 s_2}$ refers to the distance between the two scatterers. The total path length is thus, $d_{s_1 s_2} = d_{s_1} + d_{s_2} + d_{s_1 s_2}$; σ_{s_1} and σ_{s_2} refers to the RCS of the corresponding scatterers. $\boldsymbol{\gamma}_{s_1 s_2}$ is defined in a similar manner as (9).

It should be noted that the diffuse paths from the room adjacent to the antenna will undergo the same penetration loss from and to the glass windows as defined for the paths from smooth walls. Also, we assume that the diffuse scatterers inside the room do not interact with the diffuse scatterers outside the room on the road, and thus, $\boldsymbol{\alpha}_{\mathrm{diffuse}}^{s_1 s_2} = 0$ in that case. No diffuse scatterers are considered with $d_s, d_{s_1 s_2} < 2\,\mathrm{m}$ as these scatterers are observed to be in the near-field region of the antennas.

3) Mobile scatterers: Finally, the pedestrians and vehicles are modelled as mobile scatterers in their respective lanes with corresponding velocities. The two pedestrian lanes are located adjacent to the building walls. The initial position of the mobile scatterers indicating pedestrians in the x-dimension is uniformly and randomly distributed as $x_{s_{\mathrm{slow}}}(t=0) \sim U[x_{\min}, x_{\max}]$, which is determined by the pedestrian density λ_{slow}, where s_{slow} refers to the pedestrian index. The corresponding y-coordinate of the pedestrian scatterers is similarly derived as $y_{s_{\mathrm{slow}}} \sim U[y_{\mathrm{b1}}, y_{\mathrm{p1}}]$. The x- and y-coordinate of pedestrian lanes on the other side of the road is randomly generated based on Uniform distribution with the corresponding range $y_{s_{\mathrm{slow}}} \sim U[y_{\mathrm{p2}}, y_{\mathrm{b2}}]$; see Fig. 6 for the definition of $y_{\mathrm{b1}}, y_{\mathrm{p1}}, y_{\mathrm{p2}}$, and y_{b2}. The velocities of each pedestrian scatterer along the x-axis are determined as $v_{s_{\mathrm{slow}}} \sim U[-v_{\max}^{\mathrm{slow}}, v_{\max}^{\mathrm{slow}}]$, with maximum speed $v_{\max}^{\mathrm{slow}}$. We consider that there is no pedestrian movement along the y-axis.

In a similar manner, the scatterers representing fast-moving vehicles are distributed randomly in the x-dimension $x_{s_{\mathrm{fast}}}(t=0) \sim U[x_{\min}, x_{\max}]$ based on density λ_{fast}, where s_{fast} is the vehicle index. The y coordinate is then determined by $y_{s_{\mathrm{fast}}} \sim U[y_{\mathrm{p1}}, y_{\mathrm{p2}}]$, where $y_{\mathrm{p1}}, y_{\mathrm{p2}}$ are defined in Fig. 6. The direction of the vehicular movement is determined by its y-coordinate, showing the traffic lane that the scatterer is in, and hence the corresponding scatterer is assigned a positive or negative velocity. The speeds of the vehicles are determined by a Poisson distribution $v_{s_{\mathrm{fast}}} \sim \mathrm{Poisson}(v_{\mathrm{fast}})$, where v_{fast} corresponds to the mean speed in either direction; $v_{\mathrm{fast}} = 0$ for vehicles in the parking lane.

Each mobile scatterer is assigned an RCS, σ_{slow} and σ_{fast}, corresponding to pedestrians and vehicles respectively, and is assumed to show isotropic scattering. Only first order scattering is considered from the mobile scatterers. The polarimetric complex amplitude of a path arising from the s_{m}-th mobile scatterer, $s_{\mathrm{m}} \in \{s_{\mathrm{slow}}, s_{\mathrm{fast}}\}$, $\boldsymbol{\alpha}_{\mathrm{mobile}}^{s_{\mathrm{m}}}$ is calculated in a similar manner as the first order diffuse scattering in (8).

B. Channel generation

Once the delay, amplitude, AoA and AoD are defined for the reflected and scattered paths, they are combined with the antenna radiation patterns to yield the radio channel transfer function H_{ij} as

$$\begin{aligned} H_{ij} = & H_{ij,\mathrm{direct}} + \sum_{l=1}^{L} H_{ij,\mathrm{wall}}^{l} + \sum_{s=1}^{S_{\mathrm{diffuse}}} H_{ij,\mathrm{diffuse}}^{s} \\ & + \sum_{s_1=1}^{S_{\mathrm{diffuse}}} \sum_{s_2=1, s_2\neq s_1}^{S_{\mathrm{diffuse}}} H_{ij,\mathrm{diffuse}}^{s_1 s_2} + \sum_{s_{\mathrm{m}}=1}^{S_{\mathrm{mobile}}} H_{ij,\mathrm{mobile}}^{s_{\mathrm{m}}} \end{aligned}, \tag{12}$$

where L, S_{diffuse} and S_{mobile} correspond to the number of reflected paths from smooth walls, and the number of diffuse and mobile scatterers, respectively; $H_{ij,\mathrm{direct}}$ denotes the mutual coupling between the Tx and Rx antennas, which comes

TABLE I
LIST OF PARAMETERS FOR THE SI CHANNEL MODEL

Parameter	Value	Parameter	Value
λ_{fast}	$0.4\,\text{m}^{-1}$	W_{road}	19.4 m
λ_{slow}	$0.2\,\text{m}^{-1}$	W_{p1}	5.95 m
λ_{diffuse}	$2\,\text{m}^{-1}$	W_{p2}	2.92 m
σ_{fast}	$100\,\text{m}^2$	W_{L1}	3.67 m
σ_{slow}	$1\,\text{m}^2$	W_{L2}	3.67 m
σ_{diffuse}	$1\,\text{m}^2$	W_{L3}	3.59 m
$v_{\text{max}}^{\text{slow}}$	$1.39\,\text{ms}^{-1}$	W_{room}	8 m
v_{fast}	$5\,\text{ms}^{-1}$	D_{room}	8 m
CPR	0 dB	d_{break}	94.4 m
XPD_{V}	17 dB	XPD_{H}	17 dB

either from electromagnetic simulations or measurements of the considered IBFD relay. Each term in (12) is obtained by combining the radiation patterns of the Tx and Rx antennas with the corresponding polarimetric complex amplitude of path. The transfer function of the l-th path from the smooth wall reflections, $H^l_{ij,\text{wall}}$ is

$$H^l_{ij,\text{wall}} = \begin{bmatrix} E^{\text{Rx}}_{\text{V},i}(\phi^l_{\text{AoA}}) \\ E^{\text{Rx}}_{\text{H},i}(\phi^l_{\text{AoA}}) \end{bmatrix}^T \boldsymbol{\alpha}^l_{\text{wall}} \begin{bmatrix} E^{\text{Tx}}_{\text{V},j}(\phi^l_{\text{AoD}}) \\ E^{\text{Tx}}_{\text{H},j}(\phi^l_{\text{AoD}}) \end{bmatrix} \times e^{-j2\pi d_l f/c}, \tag{13}$$

where $E^{\text{Rx}}_{\text{V},i}$, $E^{\text{Rx}}_{\text{H},i}$, $E^{\text{Tx}}_{\text{V},j}$ and $E^{\text{Tx}}_{\text{H},j}$ correspond to the complex amplitude of the i-th receive and j-th transmit antenna in the azimuth plane for the vertical and horizontal polarisations respectively; $\cdot^T$ is the transpose of the matrix, $\boldsymbol{\alpha}^l_{\text{wall}}$ is given by (6). The same formulation applies in deriving the channel transfer functions for diffuse and mobile scatterers.

The model parameters, i.e., the density and RCS of the mobile and diffuse scatterers are manually optimised by heuristically comparing with the measured channel characteristics described in Section III. Due to the many multipath components received at the same delay bin as we consider up to second order diffuse scattering, the fading characteristics are an inherent part of the model.

C. Implementation recipe

The implementation of the channel model involves generating the scatterers, followed by calculating the path parameters, i.e., power, amplitude, AoA and AoD and finally generating the band-limited channel transfer function matrix $\boldsymbol{H}$. The model parameters are listed in Table I, with the geometrical settings defined in Fig. 6. The implementation steps are summarized as follows.

1) Simulate using an electromagnetic solver, or measure the mutual coupling between the Tx and Rx antennas of the IBFD relay.
2) Define the Tx/Rx position and the smooth building walls along the x-coordinate as well as room walls. Assign corresponding permittivities and derive their normal vectors.
3) Generate diffuse and mobile scatterers as shown in the layout in Fig. 6 and assign RCS to them based on the type of scatterers.
4) Assign velocities to the mobile scatterers depending on the traffic lane, which classifies pedestrians and vehicles.
5) Compute Fresnel reflection coefficients from the smooth walls upto N_{w}-th order reflections.
6) Identify the first and second order scattered paths from the diffuse scatterers along the smooth walls.
7) Derive the first order scattered paths from the mobile scatterers using their current position.
8) Calculate the channel transfer function as (12) combining all the paths depending on the desired system bandwidth and frequency spacing.
9) Update the position of the mobile scatterers for the next timestep.
10) Repeat steps 7)-10) for all remaining timesteps.

V. CHANNEL MODEL VALIDATION

In this section, the delay, Doppler and spatial characteristics of the SI channel generated by the proposed model are compared with the measurements; 50 different realisations of the mobile scatterers are simulated with the co-located Tx/Rx 30 cm away from the wall. The glass window next to the antenna has a permittivity $\epsilon_r = 6.5$ and the building walls along the road and adjacent room walls are defined as concrete, $\epsilon_r = 4$. As the measurement site was overlooking a side road parking bay, there is no building exactly opposite to the wall, but a smooth wall recessed from the building line by $D_{\text{park}} = 4.56$ m, corresponding to the wind shield of a car parked in the parking bay. The recessed smooth wall is modelled as glass windows with permittivity $\epsilon_r = 6.5$. The initial positions of the mobile scatterers are then generated in the respective lanes with corresponding velocities. Fig. 7 shows an exemplary geometry for a single time instant, where the diffuse scatterers are located adjacent to the smooth walls. The channel transfer functions (12) are derived for the same frequency band as measurements, i.e., between 2.45 and 2.75 GHz with 0.5 MHz resolution. The IFFT of the transfer function results in the band-limited CIRs.

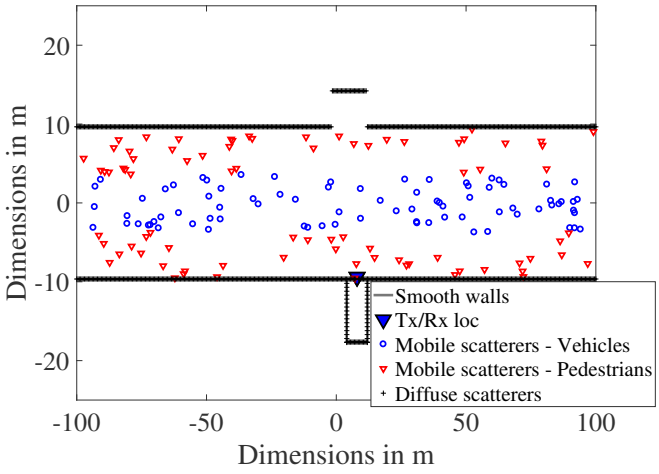

Fig. 7. Sample geometry with scatterer positions. The smooth wall opposite to the antenna is recessed to model vehicles parked in the parking bay in the side road as indicated in Fig. 4. The diffuse scatterers are located adjacent to the smooth walls. The scale along the x and y dimensions are different to each other.

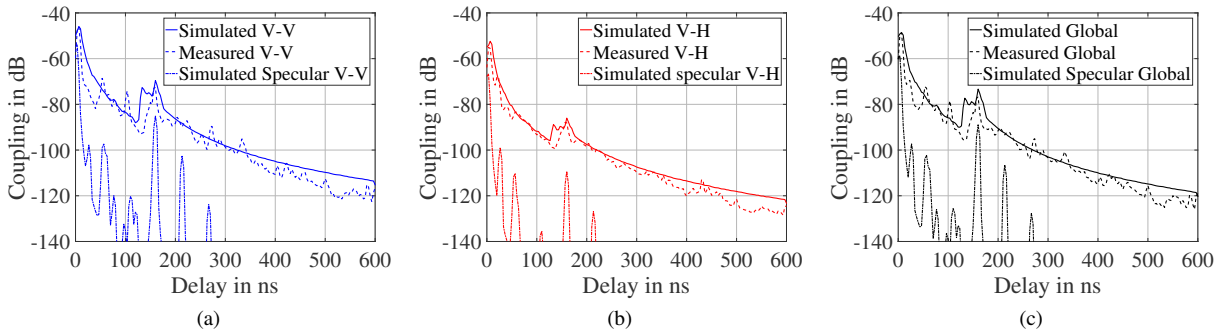

Fig. 8. Comparison of simulated and measured PDPs for (a) V-V (b) V-H polarisations of antennas and (c) *global* PDPs along with those derived from specular reflections only for the respective polarisations. The simulated PDPs for the H-H and H-V polarised combinations also follow the measurements but are not shown due to space constraint.

TABLE II
COMPARISON OF MEAN DELAY AND RMS DELAY SPREAD BETWEEN MEASUREMENTS AND SIMULATIONS

Polarization	Mean delay (ns)		RMS Delay spread (ns)	
	Measured	Simulated	Measured	Simulated
V-V	7.09	8.96	12.7	14.5
H-H	5.82	6.59	8.48	11.1
V-H	6.81	7.18	9.55	8.17
H-V	9.42	4.90	14.5	8.29
Global	6.50	7.53	10.7	12.3

A. Delay domain

Fifty CIRs are generated from each scatterer realization by adding random phases to each path to account for small-scale fading effects. The *polarisation-specific* PDPs are then calculated by incoherently averaging the 50 CIRs over different realisations of the mobile scatterers. Finally, the *global* PDPs are derived as the average of the *polarisation-specific* PDPs. Fig. 8 compares the measured and simulated PDPs according to the polarisations. The PDPs show agreement of their shapes between our simulations and measurements. The difference of the simulated and measured *global* RMS delay spread is 1.6 ns, which is less than the delay resolution of the measurement, 3.33 ns. Table II compares the simulated and measured mean delay and RMS delay spreads, indicating the validity of the model.

The fading characteristics are studied in a similar manner as described in Section III-A with the fading realizations from the 50 CIRs of the MIMO channel for different scatterer realisations. The simulated Ricean K-factors are 6.8 dB and 4.8 dB for the first two delay bins at 0 ns and 3.33 ns, compared to 5.1 dB and 0.3 dB from measurements, respectively. The remaining delay bins undergo Rayleigh fading. The small difference in the first two delay bins between the measured and simulated characteristics can be attributed to the near field scattering which is not considered in the model.

B. Doppler domain

For each of the 50 different scatterer realisations, the mobile scatterers are displaced according to their velocity, every 7 ms for 350 ms period. The paths characteristics, i.e., delay, amplitude, AoA and AoD from the mobile scatterers, are updated and the corresponding CIRs are obtained for each time step. We therefore have 50 different time-varying sets of CIRs. They are converted to the spreading functions, whereby RMS Doppler spreads are derived for each delay bin. The averaged RMS Doppler spreads over 50 different realizations of mobile scatterers and over *co-* and *cross-* polarisations of the Tx and Rx antenna feeds is shown in Fig. 9. The figure indicates good agreement between the simulated and measured RMS Doppler spreads.

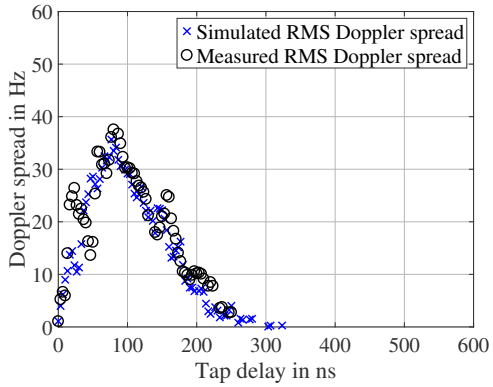

Fig. 9. Simulated and measured *global* RMS Doppler spread for each delay bin.

C. Spatial domain

Finally, we compare the simulated and measured narrowband antenna correlation on the Tx and Rx sides. The channel transfer functions at the first time step in the Doppler validation, i.e., the initial positions of the mobile scatterers defined in Section V-B, are used. The antenna correlation is calculated in a similar manner as described in Section III-C, where the average of narrowband antenna correlation values is taken over antenna elements on the other side, the radio frequency and the 50 realisations of mobile scatterers. The result gives us the same conclusion as measurements that the narrowband antenna correlation is always less than 0.6 and hence insignificant, due

to rich multipaths that both the measurements and simulations show.

VI. Conclusion

In this article, a two-dimensional site-specific GSCM was proposed for modelling the wideband dynamic MIMO SI channels for outdoor on-frequency repeater deployment. The GSCM considers smooth walls producing specular reflections, objects near the smooth walls, along with mobile scatterers like pedestrians and vehicles that create diffuse scattering. The proposed GSCM characterises the polarisation-specific SI channel in the delay, Doppler and spatial domains, and its validity was confirmed with real-world measurements at 2.6 GHz.

References

[1] S. Chen *et al.*, "Division-free duplex for wireless applications," *Electronics Letters*, vol. 34, no. 2, pp. 147–148, Jan. 1998.

[2] A. Sahai *et al.*, "Pushing the limits of full duplex wireless: design and real-time implementation," Rice Univ. Houston, TX, Tech. Rep. TREE1104, 2011. [Online]. Available: http://arxiv.org/abs/1107.0607

[3] B. P. Day *et al.*, "Full-duplex MIMO relaying: Achievable rates under limited dynamic range," *IEEE J. Sel. Areas Commun.*, vol. 30, no. 8, pp. 1541–1553, Sep. 2012.

[4] D. Bharadia *et al.*, "Full duplex radios," *SIGCOMM Comput. Commun. Rev.*, vol. 43, no. 4, pp. 375–386, Aug. 2013.

[5] D. Korpi *et al.*, "Advanced self-interference cancellation and multi-antenna techniques for full-duplex radios," in *2013 Asilomar Conf. Signals, Syst. Comput.*, Nov. 2013, pp. 3–8.

[6] A. Sabharwal *et al.*, "In-band full-duplex wireless: Challenges and opportunities," *IEEE J. Sel. Areas Commun.*, vol. 32, no. 9, pp. 1637–1652, Sep. 2014.

[7] L. Laughlin *et al.*, "Optimum single antenna full duplex using hybrid junctions," *IEEE J. Sel. Areas Commun.*, vol. 32, no. 9, pp. 1653–1661, Sep. 2014.

[8] E. Everett *et al.*, "Passive self-interference suppression for full-duplex infrastructure nodes," *IEEE Trans. Wireless Commun.*, vol. 13, no. 2, pp. 680–694, Feb. 2014.

[9] S. Hong *et al.*, "Applications of self-interference cancellation in 5G and beyond," *IEEE Commun. Mag.*, vol. 52, no. 2, pp. 114–121, feb 2014.

[10] L. Laughlin *et al.*, "Electrical balance duplexing for small form factor realization of in-band full duplex," *IEEE Commun. Mag.*, vol. 53, no. 5, pp. 102–110, May 2015.

[11] T. Huusari *et al.*, "Wideband self-adaptive RF cancellation circuit for full-duplex radio: Operating principle and measurements," in *2015 IEEE 81st Veh. Tech. Conf. (VTC Spring)*, May 2015, pp. 1–7.

[12] K. Haneda *et al.*, "Design and implementation of full-duplex transceivers," in Ch. 17 of *Signal Processing for 5G*, F.-L. Luo and C. Zhang, Eds. John Wiley & Sons, Ltd, 2016, pp. 402–428.

[13] M. Heino *et al.*, "Recent advances in antenna design and interference cancellation algorithms for in-band full duplex relays," *IEEE Commun. Mag.*, vol. 53, no. 5, pp. 91–101, May 2015.

[14] G. Liu *et al.*, "In-Band Full-Duplex Relaying: A Survey, Research Issues and Challenges," *IEEE Commun. Surv. Tutorials*, vol. 17, no. 2, pp. 500–524, 2015.

[15] M. Alleven, "Deutsche Telekom completes 5G full duplex field trial with Kumu Networks," Fierce Wireless Magazine, Sep. 2015. [Online]. Available: http://www.fiercewireless.com/tech/deutsche-telekom-completes-5g-full-duplex-field-trial-kumu-networks

[16] Geoff Carey (Mimotech), "Air division duplexing doubles transmission capacity for microwave backhaul," Presented to the Cambridge Wireless Radio Technology Special Interest Group, Bristol, U.K., July 2015. [Online]. Available: https://www.mimotechnology.com/p_microwave_carrier_ethernet.htm

[17] L. Laughlin *et al.*, "Passive and active electrical balance duplexers," *IEEE Trans. Circuits Syst. II Express Briefs*, vol. 63, no. 1, pp. 94–98, Jan. 2016.

[18] ——, "Dynamic performance of electrical balance duplexing in a vehicular scenario," *IEEE Antennas Wireless Propag. Lett.*, 2016.

[19] K. Haneda *et al.*, "Measurement of loop-back interference channels for outdoor-to-indoor full-duplex radio relays," in *Proc. Fourth European Conf. on Ant. Prop. (EuCAP 2010)*, 2010, pp. 1–5.

[20] S. N. Venkatasubramanian *et al.*, "Wideband self-interference channel modelling for an on-frequency repeater," in *10th European Conf. on Ant. Prop. (EuCAP 2016)*, Apr. 2016, pp. 1–5.

[21] J. Karedal *et al.*, "A geometry-based stochastic MIMO model for vehicle-to-vehicle communications," *IEEE Trans. Wireless Commun.*, vol. 8, no. 7, pp. 3646–3657, Jul. 2009.

[22] J. Medbo *et al.*, "Radio propagation modeling for 5G mobile and wireless communications," *IEEE Commun. Mag.*, vol. 54, no. 6, pp. 144–151, June 2016.

[23] A. F. Molisch, *Wireless Communications, 2nd Edition*. Wiley-IEEE Press, 2010.

[24] L. Greenstein *et al.*, "Moment-method estimation of the Ricean K-factor," *IEEE Commun. Lett.*, vol. 3, no. 6, pp. 175–176, June 1999.

[25] T. Riihonen *et al.*, "Mitigation of Loopback Self-Interference in Full-Duplex MIMO Relays," *IEEE Trans. Signal Process.*, vol. 59, no. 12, pp. 5983–5993, Dec. 2011.

[26] M. J. Feuerstein *et al.*, "Path loss, delay spread, and outage models as functions of antenna height for microcellular system design," *IEEE Trans. Veh. Technol.*, vol. 43, no. 3, pp. 487–498, Aug. 1994.